

Irina Ionescu
Department of Bioengineering, and
Scientific Computing and Imaging Institute,
University of Utah,
Salt Lake City, UT 84112

James E. Guilkey
Department of Mechanical Engineering,
University of Utah,
Salt Lake City, UT 84112

Martin Berzins

Robert M. Kirby

Scientific Computing and Imaging Institute,
School of Computing,
University of Utah,
Salt Lake City, UT 84112

Jeffrey A. Weiss¹
Department of Bioengineering, and
Scientific Computing and Imaging Institute,
University of Utah,
50 South Central Campus Drive,
Room 2480,
Salt Lake City, Utah 84112-9202
e-mail: jeff.weiss@utah.edu

Simulation of Soft Tissue Failure Using the Material Point Method

Understanding the factors that control the extent of tissue damage as a result of material failure in soft tissues may provide means to improve diagnosis and treatment of soft tissue injuries. The objective of this research was to develop and test a computational framework for the study of the failure of anisotropic soft tissues subjected to finite deformation. An anisotropic constitutive model incorporating strain-based failure criteria was implemented in an existing computational solid mechanics software based on the material point method (MPM), a quasi-meshless particle method for simulations in computational mechanics. The constitutive model and the strain-based failure formulations were tested using simulations of simple shear and tensile mechanical tests. The model was then applied to investigate a scenario of a penetrating injury: a low-speed projectile was released through a myocardial material slab. Sensitivity studies were performed to establish the necessary grid resolution and time-step size. Results of the simple shear and tensile test simulations demonstrated the correct implementation of the constitutive model and the influence of both fiber family and matrix failure on predictions of overall tissue failure. The slab penetration simulations produced physically realistic wound tracts, exhibiting diameter increase from entrance to exit. Simulations examining the effect of bullet initial velocity showed that the anisotropy influenced the shape and size of the exit wound more at lower velocities. Furthermore, the size and taper of the wound cavity was smaller for the higher bullet velocity. It was concluded that these effects were due to the amount of momentum transfer. The results demonstrate the feasibility of using MPM and the associated failure model for large-scale numerical simulations of soft tissue failure. [DOI: 10.1115/1.2372490]

Keywords: soft tissue, failure, material point method

Introduction

The mechanics of soft tissue failure are not well understood. The experimental data needed to develop constitutive models of failure are scarce, especially in the cases of dynamic, rate-dependent failure. The adaptation of existing failure formulations for classical engineering materials to soft tissues is complicated by the highly anisotropic nature of the materials as well as the complex geometry and deformations that accompany soft tissue failure. A framework for computational modeling of the mechanical failure of soft tissue could elucidate failure mechanisms under complex loading conditions and aid in assessing the spatial extent of material damage and failure.

There are multiple types of soft tissue trauma, and the injuries can result in very complicated effects on physiological processes associated with the injured tissues. The present work focuses on understanding the factors that control the extent of tissue damage as a result of wounding or penetrating injury. Penetrating trauma injuries are frequent, occurring in both civilian situations and in combat. They present a high socioeconomic cost and represent a significant source of morbidity [1]. A large part of the damage resulting from penetrating trauma is typically associated with damage to skeletal and cardiac muscle, ligament, tendon, and nerve. Clinical data associated with penetrating injuries are abundant, addressing wound classifications, physiology, and treatment [1–3]. However, clinical data are not sufficient to help in mechanical modeling of soft tissue failure because they do not quantify the spatial damage tissues undergo in trauma.

Although a number of experimental studies have addressed wound ballistics (e.g., [4,5]), studies explicitly addressing soft tissue failure are scarce and computational tools/frameworks for performing simulations that include soft tissue failure are nearly non-existent. Most experimental data were acquired via analyses of cadaveric tissue [6], ballistic gelatin [7,8], and physical surrogates [9]. The response of biological tissues to blunt impact [6,10] or blast [9,11,12] has been investigated. The force-time, deflection-time, and force-deflection responses of the chest to blunt ballistic impact have been documented using human cadavers [6]. High-speed photography was used to document the dynamic development of the skull fracture system in a gunshot scenario [9]. Weak blast waves have been used to investigate the relationship of the physical parameters of the waves to internal organ injury [12]. The few numerical studies that have studied soft tissue damage mechanisms have used the finite element (FE) method, because it is the most popular and widely commercially available numerical method. For instance, the response of the thoracic wall and the lung to pressure waves has been simulated using the FE method [13], which helped to elucidate the mechanisms of transmission of impact energy from the thoracic wall surface to the lung. The mechanical response of the brain to impact was investigated using the FE method [10]. None of the published work in this area have incorporated a failure model or used anisotropic constitutive models. Furthermore, the use of the FE method for modeling material failure is difficult, since changing material geometry due to failure would require constant re-meshing.

The objective of this research was to develop and test a computational framework for the analysis of soft tissue failure. A hyperelastic constitutive model with a “two-surface” strain-based failure criterion was implemented in an existing code based on the material point method (MPM) [14], a quasi-meshless numerical

¹Corresponding author.

Contributed by the Bioengineering Division of ASME for publication in the JOURNAL OF BIOMECHANICAL ENGINEERING. Manuscript received December 21, 2005; final manuscript received June 19, 2006. Review conducted by Michael Sacks.

algorithm. The implementation and performance of the constitutive and failure models were verified using simulations of simple mechanical tests (e.g., tensile and shear tests). Simulations of penetrating trauma to soft tissue samples were performed, along with sensitivity studies, analysis of the wound profile, and the resultant damage to the surrounding tissue.

Materials and Methods

Constitutive Model. The prefailure pseudoelastic material behavior of soft tissues is often approximated using hyperelastic constitutive models that allow for large deformations (e.g., [15–22]). Many biological soft tissues are composite materials, comprised of a matrix reinforced by one or more fiber families. The number and direction of fiber families dictate the local material symmetry, e.g., a single fiber family reinforcing an isotropic matrix confers transversely isotropic material symmetry [23].

In the present research, a transversely isotropic hyperelastic constitutive model was used to represent a canonical anisotropic soft tissue, comprised of an isotropic matrix reinforced by a single fiber family [24]. The local fiber direction was described by a unit vector field \mathbf{a}^0 , which changes direction and length as the material deforms:

$$\mathbf{F} \cdot \mathbf{a}^0 = \lambda \mathbf{a}, \quad (1)$$

where λ denotes the local fiber stretch, \mathbf{a} is a unit vector field representing the fiber direction after deformation, and \mathbf{F} is the deformation gradient tensor. The strain energy function W was designed with uncoupled deviatoric and volumetric terms, with separate terms for the matrix and fiber response:

$$W = F_1(\tilde{I}_1, \tilde{I}_2) + F_2(\tilde{\lambda}) + \frac{K}{2}[\ln(J)]^2, \quad (2)$$

where \tilde{I}_1 and \tilde{I}_2 are the first and second invariants of the deviatoric part of the right Cauchy-Green deformation tensor $\tilde{\mathbf{C}} = J^{-2/3} \mathbf{F}^T \mathbf{F}$ [25], $\tilde{\lambda} = \sqrt{\mathbf{a}^0 \cdot \tilde{\mathbf{C}} \cdot \mathbf{a}^0}$ is the deviatoric fiber stretch along the local direction \mathbf{a}^0 , K is the bulk modulus and $J = \det(\mathbf{F})$ is the volume ratio. The strain energy in Eq. (2) leads to the following additive decomposition for the Cauchy stress \mathbf{T} :

$$\mathbf{T} = \mathbf{T}_{\text{matrix}} + \mathbf{T}_{\text{fiber}} + \mathbf{T}_{\text{vol}}. \quad (3)$$

The matrix was represented with a neo-Hookean strain energy with material coefficient C_1 (representing the shear modulus for small deformations):

$$F_1(\tilde{I}_1, \tilde{I}_2) = C_1(\tilde{I}_1 - 3) \quad (4)$$

The elastic response of the fiber family was represented as exponential in the toe region and linear, subsequently. The actual contribution from the fiber family to the Cauchy stress is [23]:

$$\tilde{\lambda} \frac{\partial F_2}{\partial \tilde{\lambda}} = \begin{cases} 0, & \tilde{\lambda} < 1 \\ C_3 e^{C_4(\tilde{\lambda}-1)}, & \tilde{\lambda} \leq \tilde{\lambda}^* \\ C_5 \tilde{\lambda} + C_6, & \tilde{\lambda} > \tilde{\lambda}^* \end{cases} \quad (5)$$

The elastic fiber family was characterized by a coefficient C_3 that scales the exponential stresses in the toe region, a coefficient that controls the rate of fiber uncrimping C_4 , and the modulus of the straightened collagen C_5 . The stretch at which the collagen fibers straighten was denoted $\tilde{\lambda}^*$. The coefficient C_6 was determined from the condition that the stress in the collagen fibers is C^0 continuous at $\tilde{\lambda}^*$. A description of the constitutive model and its FE implementation can be found in Weiss et al. [23], whereas additional references illustrate its application [21,23,26,27].

Failure Criteria. For a composite material, the failure criteria should account for the failure mechanisms for each of the constituents [28]. Strain-based failure criteria were proposed to rep-

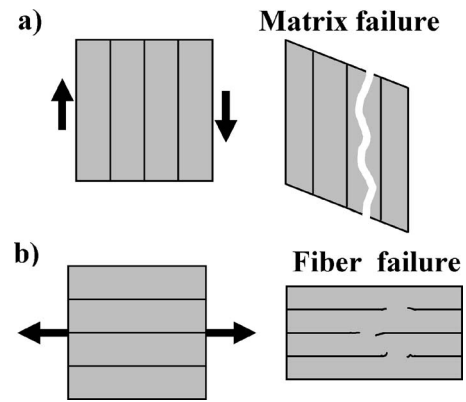


Fig. 1 Schematic indicating the two types of material failure represented in the failure model. (a) Matrix failure via shear strain. As the material strains under shear the fibers remain undeformed whereas the matrix is driven to failure, cleaving between fibers. (b) Fiber failure via elongation along the fiber direction. Under tensile strain, the “stiffer” fibers reach their stretch limit before the “softer” matrix.

resent two modes of failure: matrix failure under shear (Fig. 1(a)) and fiber failure under tension (Fig. 1(b)). Ultimate properties of soft tissue reported in the literature contain both ultimate strains and ultimate stresses [29–32]. A failure formulation based on strains was chosen because it enabled the incorporation of different failure criteria for the material components. Thus the failure criteria were defined by two failure surfaces.

Local failure of the matrix was based on the maximum Green-Lagrange shear strain γ_{max} obtained from the Green-Lagrange strain tensor \mathbf{E} :

$$\gamma_{\text{max}} = \frac{E_1 - E_3}{2}, \quad (6)$$

where E_1 and E_3 are the first and third invariants of \mathbf{E} . The matrix contribution to the stress was annulled when the shear strain in the matrix γ_{matrix} exceeded the maximum shear strain:

$$\gamma_{\text{matrix}} \geq \gamma_{\text{max}} \Rightarrow \mathbf{T}_{\text{matrix}} = \mathbf{0} \text{ and } \mathbf{T}_{\text{vol}} = \mathbf{0}. \quad (7)$$

The fiber family was considered failed locally if the fiber strain, $\varepsilon_{\text{fiber}} := \lambda - 1$, exceeded a maximum fiber strain ε_{max} . In case of failure, the fiber contribution to the total state of stress was annulled:

$$\varepsilon_{\text{fiber}} \geq \varepsilon_{\text{max}} \Rightarrow \mathbf{T}_{\text{fiber}} = \mathbf{0}. \quad (8)$$

If both of the above conditions were fulfilled locally, the material exhibited total failure at that location. An integer state variable was defined to record if and what particular type of material failure occurred.

Material Point Method. The equations of motion were discretized in space using MPM [14]. Like other quasi-meshless methods (see, e.g., [33] for a review), MPM offers an attractive alternative to traditional FE methods because it simplifies the modeling of complex geometries, large deformations, and fragmentations that are typical of soft tissue failure. MPM was chosen because numerical modeling of tissue failure using FEM is an expensive and cumbersome task, due to the need to remesh the geometry as it changes due to failure and/or contact.

Lagrangian particles or material points are used to discretize the volume of a material. Each particle carries state information about the portion of the volume that it represents, including mass, volume, velocity, stress, etc. A regular structured grid is used as a computational scratchpad for integration and solution of the weak form of the equations of motion. The domain of interest is discretized with particles. A computational grid, usually regular Car-

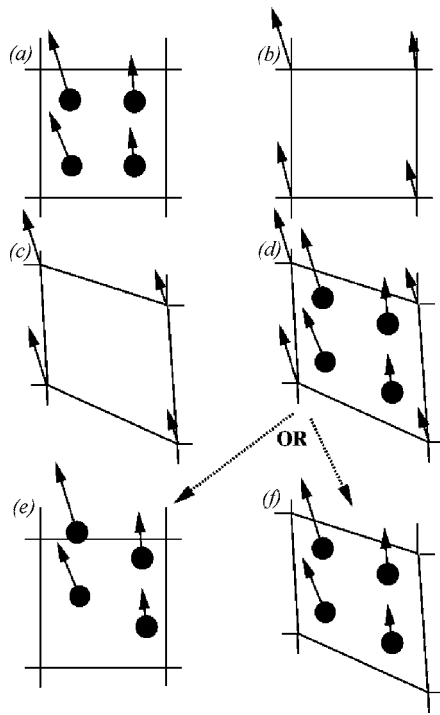


Fig. 2 Illustration of the steps in the MPM algorithm for particles occupying a single cell of the background grid. (a) A representation of four material points (filled circles), overlaid with the computational grid (solid lines). Arrows represent displacement vectors. (b) The material point state vector (mass, volume, velocity, etc.) is projected to the nodes of the computational grid. (c) The discrete form of the equations of motion is solved on the computational grid, resulting in updated nodal velocities and positions. (d) The updated nodal kinematics are interpolated back to the material points, and their state is updated. (e) In the standard MPM algorithm, the computational grid is reset to its original configuration, and the process is repeated. (f) In the modification algorithm, the grid is not reset, but is allowed to move with the particles, thereby retaining the optimal distribution of particles with respect to the grid.

tesian, is created over the entire domain (Fig. 2(a)). The physical state of the particles is projected to the computational grid using either the standard linear FE-style shape functions or some other suitable shape function [34] (Fig. 2(b)). Stress is computed at the particles based on the gradient of velocity at the nodes of the computational grid, and the equations of motion are subsequently solved on those nodes. This solution may be carried out using either explicit [14] or implicit [35] time integration. In either case, the results of the time integration are increments in the position and velocity of the nodes comprising the computational grid (Fig. 2(c)). Those increments are interpolated to the particles, and the state of the particles is updated (Fig. 2(d)).

In the traditional MPM implementation, the deformed computational grid is reset to its original undeformed configuration (Fig. 2(e)) and the simulation proceeds to the subsequent timestep. Resetting the mesh in this manner is a key feature of MPM and allows it to avoid problems of severe mesh distortion that can plague FEM simulations. The MPM mesh reset is similar to the approach used in Lagrangian kernel and other quasi-meshless methods [36]. However, for certain types of simulations, particularly quasi-static or low-rate dynamic scenarios, this step can lead to non-ideal particle distributions that may result in inaccuracies in the solution. To avoid this, one may choose not to reset the mesh at the end of a timestep (Fig. 2(f)) [37]. Using this approach, the MPM grid functions in a manner similar to a FE mesh and is

subject to the same deficiencies. However, the grid can be reset at any time to the undeformed configuration, without the difficulties of remeshing that would be required when using the FE method.

The MPM algorithm was implemented in the Uintah Computational Framework (UCF) [38], an infrastructure for large-scale parallel scientific computing on structured Cartesian grids. The UCF uses domain decomposition and the message passing interface (MPI) [39] to achieve parallelism on distributed memory clusters. Because the interactions of the particles with the computational grid are local, and due to the rectilinear structure of the background grid, parallelism of MPM is simplified. Specifically, the computational grid is easily decomposed spatially into subdomains of grid cells, with each processor performing calculations for a subdomain. When implicit time integration is used, a large system of linear equations must be solved repeatedly at each time step. The PETSC suite of linear solvers [40] was used to perform the distributed parallel solution of these equations.

When a material point fails in the MPM algorithm, the load carried by that particle is transmitted to the surrounding particles, similar to the manner in which load is transmitted from failing material to intact material in a physical specimen. As particles fail their stress or components of stress are nullified, but they remain part of the simulation, their mass contributing to the overall inertia of the material. In addition, since all particles for a given material move according to the same velocity field, failed particles tended to remain a part of the unfailed material. It is worth mentioning that in the FE method, removing the strength of an element is likely to lead to mesh distortions. To overcome this problem element erosion is used, but, in turn, this leads to mass being removed from the system.

Time Integration. Two versions of the constitutive model were implemented—one for use with explicit time integration and one for use with implicit time integration. In the explicit version, the allowable time step is computed based on cell spacing, particle velocity, and material wave speed at each particle [35]. The wave speed c is computed at each time step, based on the current value of the material density ρ and instantaneous bulk and shear moduli, K and μ ,

$$c = \sqrt{\frac{K + \mu/3}{\rho}}, \quad \text{where } \rho = \frac{\rho_0}{J}. \quad (9)$$

A necessary stability criterion for explicit time integration is the Courant-Friedrichs-Levi (CFL) condition, which requires the time step size Δt is calculated so that

$$\Delta t < \frac{\Delta x}{c}, \quad (10)$$

where Δx represents the initial size of an edge of the background grid cells. Equivalently, a CFL number may be defined as

$$\text{CFLN} = \frac{c\Delta t}{\Delta x}, \quad (11)$$

and the CFL condition then requires that Δt is chosen so $\text{CFLN} < 1.0$.

The algorithm for implicit time integration is described in Guilkey and Weiss [35]. For implicit time integration, the stiffness matrix is required to iterate to a converged solution at each time/load increment. For a hyperelastic material, the stiffness matrix is computed from the elasticity tensor \mathbf{C} [41]. The implementation of the constitutive model for implicit time integration computed both the Cauchy stress and the elasticity tensor. As with the Cauchy stress in Eq. (3), the spatial version of the elasticity tensor \mathbf{C} can be decomposed as:

$$\mathbf{C} = \mathbf{C}_{\text{vol}} + \mathbf{C}_{\text{matrix}} + \mathbf{C}_{\text{fiber}}. \quad (12)$$

In case of failure, the elasticity tensor and, thus, the stiffness matrix was reduced to represent the response of the intact material constituent.

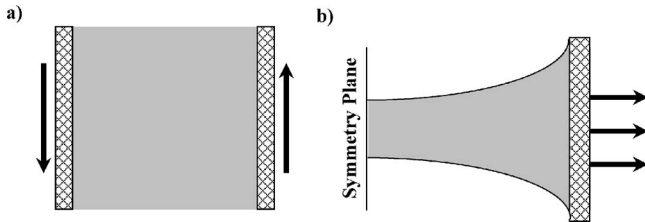


Fig. 3 Geometries used for simulating mechanical tests. (a) Along-fiber shear, a thin square specimen was deformed to failure with the help of two rigid drivers moving in opposite directions. The collagen fibers were oriented along the shearing direction, resulting in large in-plane shear strain and minimal fiber strain. (b) Tensile test, a tapered tensile test specimen was stretched to failure along the direction of the fiber family. Symmetry boundary conditions were enforced on the half model.

One Particle Test. To verify correct implementation of the constitutive model, the subfailure response of a single material point to homogeneous uniaxial elongation was examined. MPM predictions using both explicit and implicit time integration were compared to analytical solutions for an incompressible, transversely isotropic material. Separate simulations were carried out with the fiber orientation aligned with the direction of the extension and transverse to the direction of extension. The following material coefficients were used: $C_1=2.1$ KPa, $C_3=0.14$ KPa, $C_4=22$, $C_5=100$ KPa, based on myocardium properties [24], with a stretch at which the collagen fibers straighten taken arbitrarily as $\lambda^*=1.3$, and a bulk modulus of $K=100$ KPa to simulate nearly incompressible behavior.

Shear Test with Failure. The objective of this test problem was to examine the behavior of the failure model when matrix failure was initiated before fiber failure and to compare solutions for explicit and implicit time integration. A square thin sheet ($50 \times 50 \times 1$ mm) was sheared to failure with the aid of two rigid wedges (Fig. 3(a)). The fiber direction was specified as parallel to the direction of shear. Fiber stretch is minimal under this configuration, ensuring that matrix failure would be the dominant mode of material failure. The prefailure material coefficients were identical to those used in the single particle test described above. The failure of fibers was characterized by a maximum fiber strain of 0.40, and the shear strain limit for the matrix was chosen to be 0.25; the choice of these values was based on limited data in the literature [42,43] and to ensure that shear failure of the matrix would occur before fiber failure. The sheet and the drivers were assumed to be perfectly bonded. The wedges moved apart at a speed of 0.1 m/s. The material behavior of the failure model was compared to the predictions given by a model without failure in order to verify the validity of the locations of failure initiation and the type of failure observed. Solutions were obtained using both explicit and implicit time integration. After preliminary grid convergence studies, a particle resolution of $4 \times 4 \times 4$ particles per 1 mm^3 grid cell was used, yielding a total of 160,000 particles. The simulations were performed under the plane stress assumption. To aid in assessing the failure patterns, an additional analysis was performed without the failure model, establishing the distribution of maximum shear strain in the sample. Analyses were performed using 16 processors (8 nodes) of an Opteron cluster.

Tensile Test with Failure. The objective of this test problem was to examine the behavior of the failure model when fiber failure was initiated first and to compare solutions using the traditional MPM algorithm with those obtained with the modified algorithm that does not reset the background grid [37]. The geometry of a dog-bone tensile specimen (45 mm long, 10 mm wide) was discretized using a model with a single plane of symmetry to simulate a tensile test to failure (Fig. 3(b)). The fiber

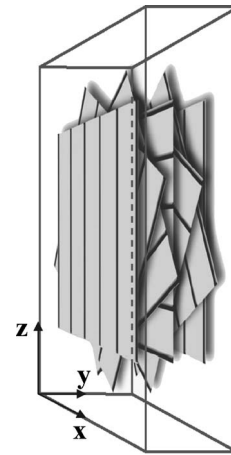


Fig. 4 Schematic of the material symmetry that was used for the projectile penetration simulations of a myocardial slab. The local fiber direction rotated 180 deg through the thickness of the slab.

direction was aligned with the testing direction. The material coefficients were based on published data for the human medial collateral ligament [21]: $C_1=1.44$ KPa, $C_3=0.57$ KPa, $C_4=48$, $C_5=467$ KPa, and $\lambda^*=1.06$. The failure of fibers was characterized by a maximum fiber strain of 0.10, and the failure of the matrix was governed by a maximum shear strain of 0.25. The use of these material coefficients for human medial collateral ligament ensured that fiber failure would precede matrix failure. The specimen was stretched to failure at a speed of 0.01 m/s. To determine whether the predicted failure location and pattern was sensitive to whether or not the computational grid was reset during the calculations, simulations were carried out using both the traditional MPM algorithm and the modified algorithm without resetting the background grid [37]. Explicit time integration was used for both analyses. A particle resolution of $4 \times 4 \times 4$ particles per 1 mm^3 grid cell was used, yielding a total of 30,000 particles. The simulations were performed under the plane stress assumption, considering a model thickness of one grid cell. Analyses were performed using 16 processors (8 nodes) of an Opteron cluster.

Slab Penetration Simulations. To investigate the behavior of the MPM failure implementation under high-rate dynamic conditions, the ballistic wounding scenario of a specimen of myocardial tissue was simulated. The material coefficients were $C_1=2.1$ KPa, $C_3=0.14$ KPa, $C_4=22$, and $C_5=100$ KPa and the stretch at which the collagen fibers straighten was assigned a value of $\lambda^*=1.4$ [24,44]. The material was considered as slightly compressible, with a bulk:shear modulus ratio of 47.6. To represent the material symmetry exhibited by the myocardium, the fiber direction a^0 was varied through the thickness of the slab so that the fiber direction rotated clockwise 180 deg from epicardial to endocardial surface [45] (Fig. 4). A $50 \times 10 \times 50$ mm myocardial slab was considered. Displacements of the edges of the slab were fixed, while the faces were free of constraints.

A 9 mm diam fragment was modeled as an elastic-plastic material with a neo-Hookean strain energy for the elastic response, with material properties based on elemental lead (bulk modulus $K=46$ GPa, shear modulus $\mu=5.6$ GPa, yield stress=18 MPa, density $\rho=11,340 \text{ kg/m}^3$ [46]). Bullet velocities of 50 m/s and 150 m/s were examined. These velocities are in the “low-speed” range of bullet velocities, i.e., <305 m/s. Low-speed projectiles produce most of their damage by crushing, with minimal damage from cavitation [1,5]. Frictional contact was modeled between the bullet and the soft tissue with a coefficient of friction of 0.08,

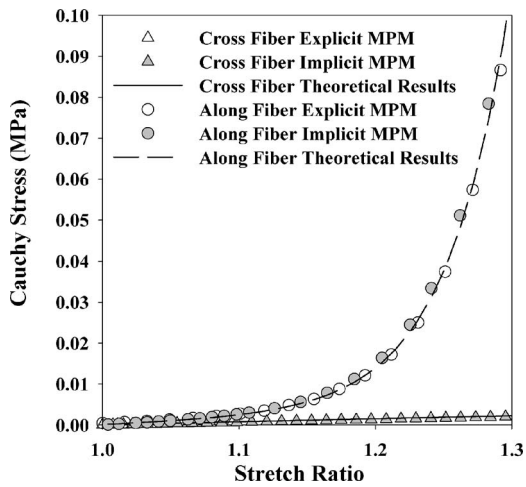


Fig. 5 Theoretical and MPM predictions for fiber stress versus strain during uniaxial extension. Separate simulations were carried out with the fiber orientation aligned with the direction of the extension and transverse to the direction of extension. Excellent agreement was obtained between the theoretical and MPM predictions using both explicit and implicit time integration.

based on the value for metal in water [47]. Frictional contact with sliding and separation was represented using our published algorithm [48].

All simulations used 1.6 million material points for discretization. To assess the influence of the resolution of the background grid, two grids were considered using the same material point discretization. A grid with a cell size of $1 \times 1 \times 1$ mm and a particle density of 64 particles per cell was referred to as the low-resolution grid, whereas a finer grid with a cell size of $0.5 \times 0.5 \times 0.5$ mm and a corresponding particle density of eight particles per cell, was referred to as the high resolution grid.

The interactions between the particles and nodes were accomplished using an interpolation method known as GIMP ((generalized interpolation material point) method [34]). When this method is used, the spatial extent of influence of each particle is finite, rather than the Dirac delta function representation that is assumed in traditional MPM. This choice leads to a more robust solution for large deformation problems at a slightly increased computational cost.

Explicit time integration was used, resetting the computational grid after each time step. The stability of the solution based on explicit time integration was investigated by performing a sensitivity study to compare the predictions for different CFL numbers: 0.1, 0.4, 0.8, and 1.0. Simulations were executed on 16 processors (8 nodes) of an Opteron cluster.

Physical elements related to the appearance of the wound were examined: geometry of the exit wound, shape of the wound tract, and size of the wound, as there are numerous clinical studies describing these factors [1,2,4].

Results

One Particle Test. Very good agreement was obtained between the theoretical predictions for a fully incompressible material and the MPM predictions, using both explicit and implicit time integration (Fig. 5). The deviations between the MPM predictions and analytical solutions were $<3\%$. These small deviations are due to dynamic effects present in the simulations that were not part of the theoretical solution. As expected, the tensile stress was substantially higher for simulations of stretch along the fiber direction than transverse to the fiber direction. The upwardly concave toe

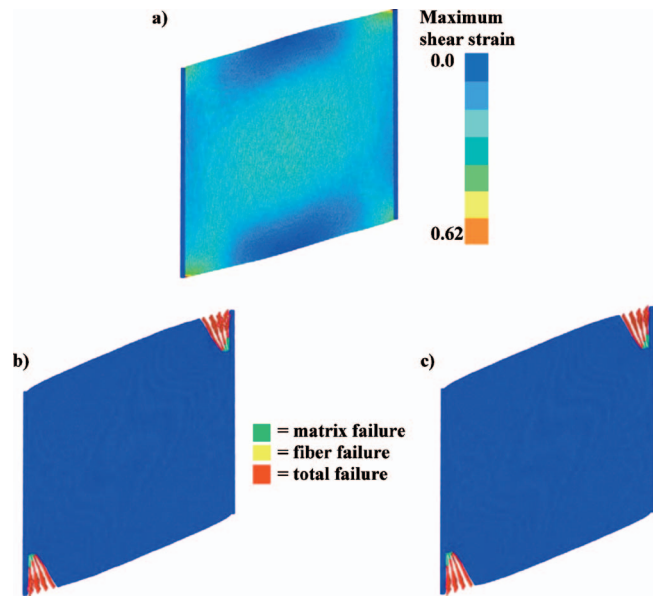


Fig. 6 Shear strain and failure patterns for simulations of a thin sheet under along-fiber shear, using both explicit and implicit time integration. (a) Maximum shear strain for the model just before initiation of failure. (b) Failure distribution for the model with failure, with explicit time integration. (c) Failure distribution for the model with failure, with implicit time integration. The location of the maximum shear strains in the model without failure features coincides with the location of failure initiation. At the particle level, subsequent deformation after matrix failure is reached results in total failure.

region was prominent along the fibers and nonexistent in the transverse direction. The explicit and implicit time integration models performed equally well.

Shear Tests. The maximum shear strain distribution in the model without failure corresponded to the locations of initiation of material failure in the models with failure, at the corners of the specimen under tension (Fig. 6(a)). Although all four corners showed higher shear strain than the central part of the specimen, the bottom-left and top-right corners had the maximum values for the domain. The patterns of failure obtained using explicit and implicit time integration were nearly identical. The failure pattern showed shearing failure of the material at the bottom-left and top-right corners, propagating along the fiber direction (Figs. 6(b) and 6(c), respectively). The failed particles moved according to the same kinematics as the intact material, while they were in the same “numerical neighborhood”—within two computational cells—explaining the frayed pattern of the damaged material. The failed particles were color coded, green corresponding to matrix failure, yellow to fiber failure, and red to total failure. As the material was reinforced by collagen fibers, soon after matrix failure occurred locally, fiber failure followed and total damage was recorded, explaining why the majority of particles exhibit total failure.

Tensile Tests. Because the specimen width tapered to a minimum at the center of the sample (Fig. 3(b)), the highest fiber strains stresses occurred at this location and as a result, failure initiated at the center of the specimen. The strain pattern shown (Fig. 7(a)) corresponds to the modified MPM algorithm simulation. The simulations using the traditional MPM algorithm and the modified algorithm that did not reset the background grid were in very good agreement, producing similar patterns of strain distributions and of failed particles (Figs. 7(b) and 7(c)). However, failure began slightly earlier in the case in which the grid was

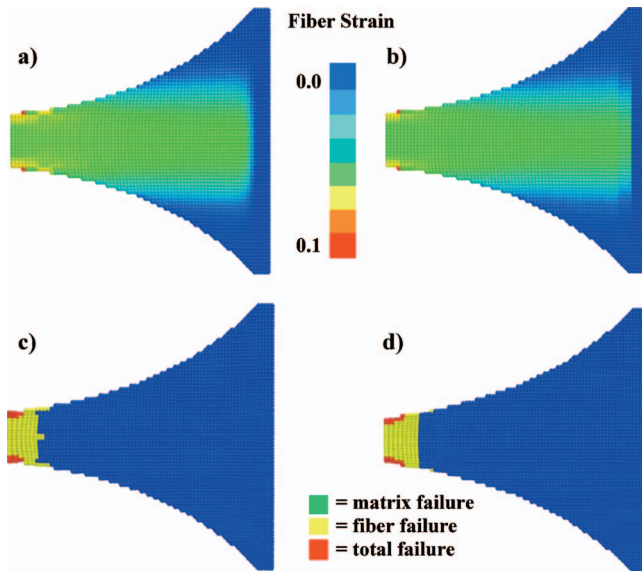


Fig. 7 Fiber strain and failure patterns for simulations of a tensile test using explicit time integration. (a) and (b) Fiber strain for grid reset and no grid reset cases, respectively, immediately before failure. (c) and (d) Failure distributions for the grid reset and no grid reset cases, respectively. Failure initiated at the location of the maximum fiber strain. As the material was fiber-reinforced, once the fibers failed, total material failure followed.

reset. As the specimen elongated, fiber failure was initiated first, followed by total failure, as the matrix was unable to maintain the total force after the reinforcing fibers failed.

Slab Penetration Simulations. The simulation that used the higher-resolution background grid produced an exit wound with a more realistic appearance, by comparison to clinical descriptions of ballistic wounds [1,2,4]. The low-resolution grid resulted in an exit wound with a jagged edge, revealing the contours of the underlying Cartesian computational grid (data not shown). The artifact became less prominent with increasing grid resolution. Based on these results, the higher-resolution grid was used for subsequent simulations. A mesh convergence study showed no change in results with further mesh refinement.

Different values of the Courant number produced slight variations in the appearance of the exit wound. These data were used to establish the Courant number that was necessary to obtain both accurate and stable solutions. Based on the results, a value of 0.1 was used for subsequent simulations, ensuring better accuracy at the expense of more computational expense.

Figure 8 shows a time sequence of images for the bullet penetration of a myocardial slab.

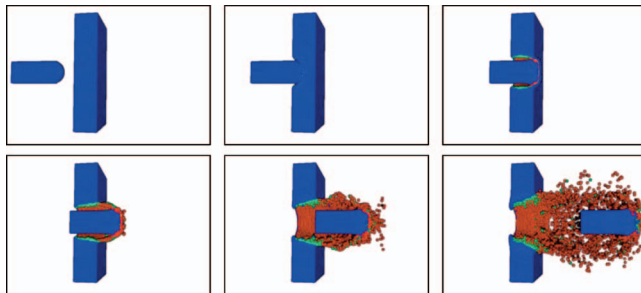


Fig. 8 Time sequence of images for the projectile penetration of a myocardial slab. Bullet velocity was 50 m/s. Colors indicate failure status of material points: blue = no failure, green = matrix failure, yellow = fiber failure, red = total failure.

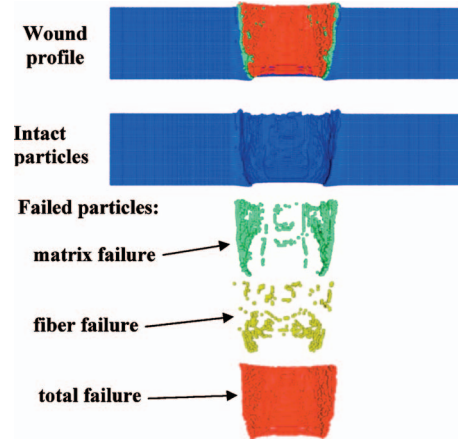


Fig. 9 Wound profile for the projectile penetration of a myocardial slab. The wound profile shows a central area of complete tissue disruption surrounded by layers of failed particles. The wound tract presents a diameter increase from entrance to exit. Initial bullet velocity was 50 m/s.

etrating the myocardial slab. These data were obtained from the low-velocity simulations with a Courant number of 0.1, using the fine grid resolution. As the bullet penetrated the slab, it transferred its energy to the surrounding tissue producing damage [4]. The increasing size of the wound with distance from the entrance location is evident. Plastic yielding at the tip of the bullet can be seen in the lower panels.

For all slab penetration simulations, the wound profile exhibited an approximate circular central area of complete tissue disruption in the fragment path, presenting a diameter increase from entrance to exit, as reported in clinical cases [4] (Fig. 9). A layered distribution of the failed particles was observed in the adjoining area of “injured” soft tissue. As expected, the number of failed particles decreased with distance from the center of the bullet tract. The percentage of failed particles was $\sim 5\%$ of the total number of particles.

The distribution of failed particles, the size of the entry wound and cavity, and the shape of the exit wound depended on the speed of the projectile. A speed of 150 m/s produced an almost round exit wound, with evenly distributed layers of failed particles (Fig. 10(a)), whereas a lower speed of 50 m/s produced an elliptical distribution of failed particles (Fig. 10(b)), reflecting the underlying symmetry of the fiber family and its variation through the slab (Fig. 4). Thus, the influence of the transversely isotropic material symmetry was more pronounced at lower projectile velocities.

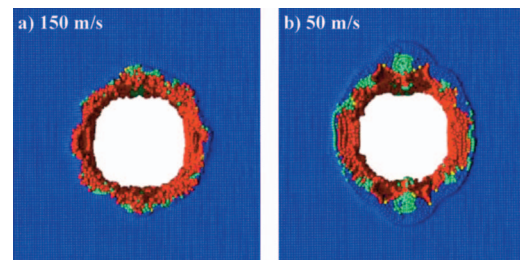


Fig. 10 Influence of projectile speed on the exit wound. Figure 4 shows the local fiber direction for the simulation. The appearance of the exit wound shows that the material symmetry had a greater influence at lower projectile speeds than at higher speeds. The failed particles were distributed randomly in the case of the injury at a higher speed (a), whereas in the lower-speed case (b) the failure pattern reflected the underlying fiber orientation.

The size of the entry wound was between 10 mm and 11 mm. For the 50 m/s simulation, the diameter of the resulting cavity was between 16 mm and 19 mm, whereas the diameter of the cavity plus the layer of failed material was between 29 mm and 38 mm.

The wall clock time required to complete each of the slab penetration simulations with the fine computational grid and a CFLN of 0.1 varied between 24 hr and 48 hr, depending on bullet velocity.

Discussion

A computational framework for assessing soft tissue failure was developed using a transversely isotropic hyperelastic constitutive model, a two-surface failure model, and the MPM numerical framework. The strain-based failure model accommodated different failure modes for a fiber family and the matrix. Numerical experiments were performed using explicit and implicit time integration to verify the implementation and to ensure that predictions of failure were not affected by the type of numerical time integration. Results of the ballistic simulations have shown a realistic wound tract that reflects the geometry of wound tracts observed in experimental studies. The failure criteria permitted quantification of the spatial distribution and type of damage experienced by the soft tissue.

Simulations of shear loading and tensile loading isolated the two different failure criteria and illustrated the resulting propagation of failure through the tissue. In the shear loading example, the resulting strain state consisted primarily of deviatoric strain, while fiber strain was minimal. This resulted in failure at the locations of maximum shear strain in the matrix. In the case of the tensile test, the strain field consisted again primarily of deviatoric strain, but in this case the fiber strain was dominant. Thus, fiber failure was initiated first, followed subsequently by failure of the matrix and thus total failure. These simulations demonstrate the ability of the implementation to predict expected patterns of failure for well-defined loading conditions.

The simulations that examined projectile penetration of a myocardial slab demonstrate the utility of this computational framework for large-scale, relatively high-rate simulations. For these problems, the scalability of the MPM algorithm to hundreds of processors provides a framework that can examine extremely large and detailed simulations. The predictions of exit and entry wound size, and the trends with increases in velocity are consistent with published experimental data [2,4]. The velocity of the projectile affected the influence of the material symmetry on the appearance of the exit wound as well as the diameter of the wound cavity. Both these phenomena are likely related to the amount of momentum transfer that occurs. Specifically, for this particular simulation, a slower bullet velocity results in more momentum transfer to the material. Detailed experimental data are needed to validate these numerical results and constitute the objective of future work. Ballistic gelatin experiments may provide a controlled framework for gathering information about the way the damage propagates through the tissue and the rate dependence of the results [7,8].

The main advantages of the MPM framework for both low-rate and high-rate failure simulations are the ease with which complicated geometries can be represented, the ability to implement arbitrary constitutive models and the ability to circumvent mesh entanglement and inversion problems that can occur with the FE method. Large computations are easily accommodated, with excellent parallel scaling [37]. The simulation of ballistic soft tissue injury demonstrated the capability of MPM framework to solve large, high-rate dynamic problems. The same problem would have been much more difficult to analyze using the FE method, as remeshing would have been needed to avoid mesh entanglement and element inversion. The standard MPM algorithm eliminates element inversion by using a computational grid that is reset after each time step. In the case of the standard FE method, mesh inversion can be mitigated by using adaptive mesh refinement

(AMR) (or “h-refinement,” e.g., [49]). However, AMR introduces additional difficulties since an optimal new mesh is ill-defined and interpolation errors are introduced when projecting to a new mesh. The process of generating the new mesh is plagued by the same difficulties as occur when generating the initial mesh, and this process is especially difficult in three dimensions. When compared to generating an entirely new FE mesh for use with AMR, the process of resetting the MPM background grid is trivial.

The main weaknesses of the present research are the relative simplicity of the failure and a lack of available experimental data to determine failure criteria. Failure predictions are specific to the chosen failure criteria. Failure criteria that take into account multiple models of failure need to be developed and implemented. Only two modes of failure have been incorporated, assuming an additive decomposition of the Cauchy stress into collagen fiber response and ground matrix response. The interaction between fibers and matrix [23,28,50] has not been taken into account in the prefailure constitutive model or the failure model. The choice of failure parameters was based on published data found for soft tissues but does not represent actual values. Soft tissue response to impact and trauma has been numerically investigated using FE [10,13]; however, as previously mentioned, to our knowledge this is the only computational model explicitly incorporating failure criteria. A more comprehensive failure criterion is needed in order to assess the way the damage propagates in the surrounding tissue as a result of trauma, for example the influence of wounding on the adjacent blood vessels, and accounting for the subsequent swelling of the tissue.

The propagation of shock waves in soft tissue for high-velocity injury scenarios is another topic that still needs to be addressed. The presence of shock waves that precede the projectile is indicated by cavitation. Experimental data for low-speed projectile injuries show there is minimal or no evidence of cavitation [1,5]. However, in the case of high-velocity projectile injuries, the phenomenon of cavitation can be significant (the projectile advances in a temporary cavity rather than directly through the tissue) [5]. This will require detailed experimental testing, as experimental data are needed in order to develop a more comprehensive failure model and to account for viscoelastic effects [27]. The addition to the model of viscoelasticity and appropriate failure formulations would enable the study of transient effects occurring in “high-speed” (>304.8 m/s) projectile injuries, i.e., cavitation, shock wave propagation, as well as rate-dependency effects in the material in both low- and high-speed injury scenarios. These additions would certainly improve the fidelity of the predictions, as it is possible that tissue viscoelasticity may serve as an additional dissipative mechanism and could significantly alter model predictions during high-rate loading.

In summary, this study has demonstrated the feasibility of using MPM and the associated failure model for large-scale simulations of soft tissue failure. The present framework allows for the straightforward implementation of alternative constitutive models and failure formulations, and the results obtained for the test problems are realistic and encouraging.

Acknowledgment

This work was supported by a grant from DARPA, executed by the U.S. Army Medical Research and Materiel Command/TATRC Cooperative Agreement, Contract No. W81XWH-04-2-0012, and by the U.S. Department of Energy through the Center for the Simulation of Accidental Fires and Explosions, under Grant W-7405-ENG-48. A grant of computer time on the Arches Metacluster was provided by the Center for High Performance Computing, University of Utah. The Arches Metacluster was funded by NIH Grant No. RR17214-01. The authors thank the staff of the Scientific Computing and Imaging Institute and the Center for the Simulation of Accidental Fires and Explosions at the University of Utah for assistance with software development.

References

- [1] Gugala, Z., and Lindsey, R. W., 2003, "Classification of Gunshot Injuries in Civilians," *Clin. Orthop. Relat. Res.*, **1**, pp. 65–81.
- [2] Fackler, M. L., 1996, "Gunshot Wound Review," *Ann. Emerg. Med.*, **28**, pp. 194–203.
- [3] Davis, R. E., Bruno, 2nd, A. D., Larsen, W. B., Sugimoto, J. T., and Gaines, R. D., 2005, "Mobile Intrapericardial Bullet: Case Report and Review of the Literature," *J. Trauma: Inj., Infect., Crit. Care*, **58**, pp. 378–380.
- [4] Bartlett, C. S., 2003, "Clinical Update: Gunshot Wound Ballistics," *Clin. Orthop. Relat. Res.*, **1**, pp. 28–57.
- [5] Sellier, K. G., and Kneubuehl, B. P., 1994, *Wound Ballistics - And the Scientific Background*, Elsevier, New York.
- [6] Bir, C., Viano, D., and King, A., 2004, "Development of Biomechanical Response Corridors of the Thorax to Blunt Ballistic Impacts," *J. Biomech.*, **37**, pp. 73–79.
- [7] Korac, Z., Kelenc, D., Baskot, A., Mikulic, D., and Hancevic, J., 2001, "Substitute Ellipse of the Permanent Cavity in Gelatin Blocks and Debridement of Gunshot Wounds," *Mil. Med.*, **166**, pp. 689–694.
- [8] Ragsdale, B. D., and Josselson, A., 1988, "Predicting Temporary Cavity Size From Radial Fissure Measurements in Ordnance Gelatin," *J. Trauma*, **28**, pp. S5–S9.
- [9] Thali, M. J., Kneubuehl, B. P., Vock, P., Allmen, G., and Dirnhofer, R., 2002, "High-Speed Documented Experimental Gunshot to a Skull-Brain Model and Radiologic Virtual Autopsy," *Am. J. Forensic Med. Pathol.*, **23**, pp. 223–228.
- [10] Brands, D., 2002, *Predicting Brain Mechanics During Closed Head Impact: Numerical and Constitutive Aspects*, Eindhoven Technical University, University Press Facilities, Eindhoven, The Netherlands.
- [11] Josephson, L. H., and Tomlinson, P., 1988, "Predicted Thoraco-Abdominal Response to Complex Blast Waves," *J. Trauma*, **28**, pp. S116–S124.
- [12] Yang, Z., Wang, Z., Tang, C., and Ying, Y., 1996, "Biological Effects of Weak Blast Waves and Safety Limits for Internal Organ Injury in the Human Body," *J. Trauma: Inj., Infect., Crit. Care*, **40**, pp. S81–S84.
- [13] Grimal, Q., Gama, B. A., Naili, S., Watzky, A., and Gillespie, Jr., J. W., 2004, "Finite Element Study of High-Speed Blunt Impact on Thorax: Linear Elastic Considerations," *Int. J. Impact Eng.*, **30**, pp. 665–683.
- [14] Sulsky, D., Chen, Z., and Schreyer, H. L., 1994, "Particle Method for History-Dependent Materials," *Comput. Methods Appl. Mech. Eng.*, **118**, pp. 179–196.
- [15] Pena, E., Calvo, B., Martinez, M. A., and Doblare, M., 2006, "A Three-Dimensional Finite Element Analysis of the Combined Behavior of Ligaments and Menisci in the Healthy Human Knee Joint," *J. Biomech.*, **39**, pp. 1686–1701.
- [16] Omens, J. H., McCulloch, A. D., and Criscione, J. C., 2003, "Complex Distributions of Residual Stress and Strain in the Mouse Left Ventricle: Experimental and Theoretical Models," *Biomech Model Mechanobiol.*, **1**, pp. 267–277.
- [17] Seshaiyer, P., and Humphrey, J. D., 2003, "A Sub-Domain Inverse Finite Element Characterization of Hyperelastic Membranes Including Soft Tissues," *ASME J. Biomech. Eng.*, **125**, pp. 363–371.
- [18] Guccione, J. M., McCulloch, A. D., and Waldman, L. K., 1991, "Passive Material Properties of Intact Ventricular Myocardium Determined From a Cylindrical Model," *ASME J. Biomech. Eng.*, **113**, pp. 42–55.
- [19] Vorp, D. A., Rajagopal, K. R., Smolinski, P. J., and Borovetz, H. S., 1995, "Identification of Elastic Properties of Homogeneous, Orthotropic Vascular Segments in Distension," *J. Biomech.*, **28**, pp. 501–512.
- [20] Criscione, J. C., Sacks, M. S., and Hunter, W. C., 2003, "Experimentally Tractable, Pseudo-Elastic Constitutive Law for Biomembranes: II. Application," *ASME J. Biomech. Eng.*, **125**, pp. 100–105.
- [21] Gardiner, J. C., and Weiss, J. A., 2003, "Subject-Specific Finite Element Analysis of the Human Medial Collateral Ligament During Valgus Knee Loading," *J. Orthop. Res.*, **21**, pp. 1098–1106.
- [22] Prendergast, P. J., Lally, C., Daly, S., Reid, A. J., Lee, T. C., Quinn, D., and Dolan, F., 2003, "Analysis of Prolapse in Cardiovascular Stents: A Constitutive Equation for Vascular Tissue and Finite-Element Modelling," *ASME J. Biomech. Eng.*, **125**, pp. 692–699.
- [23] Weiss, J. A., Maker, B. N., and Govindjee, S., 1996, "Finite Element Implementation of Incompressible, Transversely Isotropic Hyperelasticity," *Comput. Methods Appl. Mech. Eng.*, **135**, pp. 107–128.
- [24] Humphrey, J. D., Strumpf, R. K., and Yin, F. C. P., 1990, "Determination of a Constitutive Relation for Passive Myocardium. II. Parameter Estimation," *ASME J. Biomech. Eng.*, **112**, pp. 340–346.
- [25] Spencer, A., 1980, *Continuum Mechanics*, Longman, New York.
- [26] Quapp, K. M., and Weiss, J. A., 1998, "Material Characterization of Human Medial Collateral Ligament," *ASME J. Biomech. Eng.*, **120**, pp. 757–763.
- [27] Puso, M. A., and Weiss, J. A., 1998, "Finite Element Implementation of Anisotropic Quasi-Linear Viscoelasticity Using a Discrete Spectrum Approximation," *ASME J. Biomech. Eng.*, **120**, pp. 62–70.
- [28] Hinton, M., Soden, P., and Kaddour, A., 2004, *Failure Criteria in Fibre-Reinforced Polymer Composites*, Elsevier, New York.
- [29] Haut Donahue, T. L., Gregersen, C., Hull, M. L., and Howell, S. M., 2001, "Comparison of Viscoelastic, Structural, and Material Properties of Double-Looped Anterior Cruciate Ligament Grafts Made From Bovine Digital Extensor and Human Hamstring Tendons," *ASME J. Biomech. Eng.*, **123**, pp. 162–169.
- [30] Pini, M., Zysset, P., Botsis, J., and Contro, R., 2004, "Tensile and Compressive Behaviour of the Bovine Periodontal Ligament," *J. Biomech.*, **37**, pp. 111–119.
- [31] Moore, S. M., McMahon, P. J., Azemi, E., and Debski, R. E., 2005, "Bi-directional Mechanical Properties of the Posterior Region of the Glenohumeral Capsule," *J. Biomech.*, **38**, pp. 1365–1369.
- [32] Hashemi, J., Chandrashekar, N., and Slauterbeck, J., 2005, "The Mechanical Properties of the Human Patellar Tendon are Correlated to its Mass Density and are Independent of Sex," *Clin. Biomech. (Los Angel. Calif.)*, **20**, pp. 645–652.
- [33] Li, S., 2002, "Meshfree and Particle Methods and Their Applications," *Appl. Mech. Rev.*, **55**, pp. 1–34.
- [34] Bardenhagen, S. G., and Kober, E. M., 2004, "The Generalized Interpolation Material Point Method," *Comput. Model. Eng. Sci.*, **5**, pp. 477–496.
- [35] Guilkey, J. E., and Weiss, J. A., 2003, "Implicit Time Integration for the Material Point Method: Quantitative and Algorithmic Comparisons With the Finite Element Method," *Int. J. Numer. Methods Eng.*, **57**, pp. 1323–1338.
- [36] Belytschko, T., Guo, Y., Liu, W. K., and Xiao, S. P., 2000, "A Unified Stability Analysis of Meshless Particle Methods," *Int. J. Numer. Methods Eng.*, **48**, pp. 1359–1400.
- [37] Guilkey, J. E., Hoying, J. B., and Weiss, J. A., 2006, "Computational Modeling of Multicellular Constructs With the Material Point Method," *J. Biomech.*, **39**, pp. 2074–2086.
- [38] Parker, S. G., 2002, "A Component-Based Architecture for Parallel Multiphysics PDE Simulation," *ICCS2002 Workshop on PDE Software*, Sloot, P. M. A. et al., eds., Springer-Verlag, Lecture Notes in Computer Science, Berlin, 2331, pp. 719–734.
- [39] Gropp, W., Lusk, E., Doss, N., and Skjellumb, A., 1996, "A High-Performance, Portable Implementation of the MPI Message Passing Interface Standard," *Parallel Comput.*, **22**, pp. 789–828.
- [40] Balay, S., Buschelman, K., Gropp, W., Kaushik, D., Knepley, M., Curfman McInnes, L., Smith, B., and Zhang, H., 2001, "PETSc," in <http://www.mcs.anl.gov/petsc>
- [41] Holzapfel, G. A., 2001, *Nonlinear Solid Mechanics: A Continuum Approach for Engineering*, Wiley, New York.
- [42] Hunter, P. J., McCulloch, A. D., and ter Keurs, H. E., 1998, "Modelling the Mechanical Properties of Cardiac Muscle," *Prog. Biophys. Mol. Biol.*, **69**, pp. 289–331.
- [43] Humphrey, J. D., 2002, *Cardiovascular Solid Mechanics. Cells, Tissues, and Organs*, Springer-Verlag, Berlin.
- [44] Veress, A. I., Gullberg, G. T., and Weiss, J. A., 2005, "Measurement of Strain in the Left Ventricle During Diastole with Cine-MRI and Deformable Image Registration," *ASME J. Biomech. Eng.*, **127**, pp. 1195–1207.
- [45] Omens, J. H., MacKenna, D. A., and McCulloch, A. D., 1993, "Measurement of Strain and Analysis of Stress in Resting Rat Left Ventricular Myocardium," *J. Biomech.*, **26**, pp. 665–676.
- [46] Automation Creations, 2004, "Material Property Data," in <http://www.matweb.com>
- [47] Engineers Edge, 2000–2005, "Engineering, Manufacturing, Design Database and Tools," in engineersedge.com
- [48] Bardenhagen, S. G., Guilkey, J. E., Roessig, K. M., Brackbill, J. U., Witzel, W. M., and Foster, J. C., 2001, "An Improved Contact Algorithm for the Material Point Method and Application to Stress Propagation in Granular Material," *Comput. Model. Eng. Sci.*, **2**, pp. 509–522.
- [49] de Cougny, H. L., and Shephard, M. S., 1999, "Parallel Refinement and Coarsening of Tetrahedral Meshes," *Int. J. Numer. Methods Eng.*, **46**, pp. 1101–1125.
- [50] Guerín, H. A., and Elliott, D. M., 2005, "The Role of Fiber-Matrix Interactions in a Nonlinear Fiber-Reinforced Strain Energy Model of Tendon," *ASME J. Biomech. Eng.*, **127**, pp. 345–350.